PCCP

Accepted Manuscript

ROYAL SOCIETY OF CHEMISTRY

www.rsc.org/pccp

Facile synthesis of high quality nanostructured CeO_2 and Gd_2O_3-doped CeO_2 solid electrolyte for improved electrochemical performance

Yu-Lin Kuo[a,*], Yu-Ming Su[a], Hung-Lung Chou[b]

[a] *Department of Mechanical Engineering, National Taiwan University of Science and Technology, 43, Section 4, Keelung Road, Taipei, 10607, Taiwan.*

[b] *Graduate Institute of Applied Science and Technology, National Taiwan University of Science and Technology, 43, Section 4, Keelung Road, Taipei, 10607, Taiwan.*

ABSTRACT

This study describes the use of a composite nitrate salt solution as a precursor to synthesize CeO_2 and Gd_2O_3-doped CeO_2 (GDC) nanoparticles (NPs) using an atmospheric pressure plasma jet (APPJ). The microstructures of CeO_2 and GDC NPs were found to be cubical and spherical shaped nanocrystallites with average particle sizes of 10.5 and 6.7 nm, respectively. Reactive oxygen species, detected by optical emission spectroscopy (OES), are believed to be the major oxidative agents for the formation of oxide materials in the APPJ process.

Based on the material characterization and OES observations, the study effectively demonstrated the feasibility of preparing well-crystallized GDC NPs by the APPJ system as well as the gas-to particle mechanism. Notably, the Bader charge of CeO_2 and $Ce_{0.9}Gd_{0.1}O_2$ characterized by density function theory (DFT) simulation

and AC impedance measurements shows that Gd helps to increase the charge on $Ce_{0.9}Gd_{0.1}O_2$ NPs, thus improving their conductivity and making them candidate materials for electrolytes in solid oxide fuel cells.

Keywords: atmospheric pressure plasma jet (APPJ), Gd_2O_3-doped CeO_2 (GDC), nanoparticles, density function theory (DFT)

*Correspondent author: Yu-Lin Kuo

Address: No.43, Section 4, Keelung Road, Taipei 10607, Taiwan.

Tel: +886-2-27376784; Fax: +886-2-27376460

E-mail address: ylkuo@mail.ntust.edu.tw

1. INTRODUCTION

Pure stoichiometric CeO_2, which is known to be an electrical conductor, has a structure analogous to calcium fluoride (fluorite). When ceria is doped with oxides of bi- or tri-valent metals, the ionic conductivity becomes larger than the electronic conductivity; due mainly to the introduction of oxygen vacancies.

Experimental studies based on trivalent metal ions doped-ceria have received much attention due to their potential applications as electrolyte materials for solid oxide fuel cells (SOFCs). According to Kilner and Brook [1], maximum ionic conductivity in oxide fluorites could be achieved from the addition of dopant causing a minimum elastic strain in the host crystal lattice. Kim [2] proposed a concept of critical ionic radius (r_c), at which the dopant causes neither expansion nor contraction in the host fluorite oxide lattice. A cation with anionic radius equal to r_c should be the ideal dopant to show the highest ionic conductivity. Recently, Omar *et al*., [3] studied the relationship between the cation size of trivalent dopant and the ionic conductivity in doped ceria. They found the maximum ionic conductivity is achieved in Nd-doped CeO_2, instead of Gd-doped CeO_2, as predicted by Kim's critical ionic radius theory and additionally, that the migration enthalpy is dependent on the dopant type, which contradicts previously reported data [2]. They concluded that the ionic conductivity is not a function solely of elastic strain, and that r_c is not sufficient to explain the

behavior of ionic conductivity in doped ceria. Comparing the results for ceria doped with different aliovalent dopants, Gd_2O_3-doped CeO_2 (GDC) is reported to be one of the most promising solid electrolyte materials for the operation of SOFC below 700 °C [4, 5]. In the die pressing and sintering process, GDC is inherently difficult to densify below 1500 °C [6-8]. Ultrafine nanoparticles (NPs) have been proven to reduce the sintering temperature and raise the densification level (>95%) of solid electrolytes.

NP materials have been widely applied in industrial application because of their novel electronic, optical, magnetic, and catalytic properties that are radically different their bulk counterparts. Multicomponent NPs generally possess characteristics superior to their individual components, such as higher electrocatalytic activity, enhanced catalytic selectivity and physical/chemical stability [9, 10]. At present, several synthesis routes [11-13] are able to produce NPs; many reports currently described the successful preparation of single component NPs with controlled particle sizes.

Generally speaking, gas-phase and liquid-phase methods are commonly used to synthesize NPs. For the liquid-phase methods, these controlled preparations of multicomponent NPs involve several complicated procedures [14-17] and the control of various parameters, e.g. pH values, solute/solvent ratios, and reaction

temperatures/times. NPs produced by gas-phase methods have traditionally used chemical vapor deposition, which relies on toxic, pyrophoric and expensive organic volatile precursors. In addition, these gas-phase approaches are complex and have suffered from excessive particle growth and aggregation, making them far less useful than liquid phase approaches for NP synthesis.

Atmospheric-pressure plasmas techniques have been used in several applications for surface treatment [18], thin film deposition [19], and nanoparticle fabrication [20]. Here, we report the use of an atmospheric pressure plasma jet (APPJ) in conjunction with nitrate salt precursor solutions in a fast oxidation process for the one-step fabrication of CeO_2 and 10GDC NPs. So far, the synthesis of CeO_2 and GDC NPs using an atmospheric plasma process has not been investigated. In this study, the fabrication of ceria-based nanoparticles by APPJ is presented, together with a proposed formation mechanism. DFT simulation was employed for the charge analyses of CeO_2 and $Ce_{0.1}Gd_{0.9}O_2$ to highlight differences in ionic conductivity.

2. EXPERIMENTAL SETUP

2.1 APPJ Synthesis of the GDC Nanoparticles

Commercial gadolinium nitrate hexahydrate ($Gd(NO_3)_3 \cdot 6H_2O$, 99%) and cerium nitrate hexahydrate ($Ce(NO_3)_3 \cdot 6H_2O$, 99%) were purchased from Acros Organics for the NP synthesis. The APPJ systems were performed using a plasma jet head, a DC power supply, an ultrasonic generator and a gas delivery system. The precursor solution was prepared by dissolving $Gd(NO_3)_3 \cdot 6H_2O$ and $Ce(NO_3)_3 \cdot 6H_2O$ into de-ionized water to form a aqueous solution with a concentration of 0.05 M. The molar ratio of metal ions (Gd/Ce = 1/9) was marked as 10GDC in this study. During the preparation of CeO_2 and 10GDC particles, the DC power supplied to the plasma discharge was kept at 300 W, and the flow rate of clean dry air as working gas was maintained at 40 slm. The atomized precursor solution droplets were generated by a 2.45 MHz piezoelectric oscillator and subsequently transferred into the plasma region by the O_2 carrier gas with a flow rate of 1 slm. The resulting particles were then collected in de-ionized water in a pyrex beaker.

2.2 Materials Characterizations

The crystallite structure of prepared CeO_2 and 10GDC particles were verified by X-ray diffraction (XRD, Bruker D2 Phaser, Cu-Kα radiation of radiation of λ = 1.5405 Å), employing a scanning rate of 0.02 deg $\cdot$ s^{-1} in the 2θ range from 20^o to 80^o.

The structure refinement and the lattice parameters were obtained using Bruker TOPAS 4.2 software. The morphology and selected area electron diffraction (SAED) of the prepared particles were characterized using FEI Titan transmission electron microscopy (TEM) operated at 200 kV accelerating voltage. Particle size distribution from dynamic light scattering (DLS) measurements was done with Malvern Zeta Seizer instrument of Model No. NANOZA90. All the scattered photons are collected at a 90^{o} scattering angle. Optical emission spectroscopy (OES, BRC112E Series Fiber Coupled 16 Bit USB CCD Spectrometer, B&W Tek Inc., USA) was employed for the qualitative investigation of plasma species under normal pressure. An optical fiber with a lens was placed in front of the plasma region to collect light emissions directly. The electrical performance of the prepared CeO_2 and 10GDC were studied by measuring the impedance spectra of pellets in the frequency range from 0.01 Hz to 3 MHz using an impedance analyzer (Zahner, IM6ex, Germany) with ac amplitude of 10 mV at 500 and 700 °C. The pellets were prepared using a cold pressing method at 1 ton pressure and were then sintered at 1500 °C for 5 h in air. Platinum electrodes with a thickness of 70 um were secured to either sides of the sintered pellet using Heraeus CL11-5100 Platinum adhesive paste and held at 1050 °C for 1 h.

2.3 Computational Details

For the DFT calculations, we employed projector-augmented waves (PAW) [21-24] generalized gradient approximation (GGA) [25-27] as implemented in the Vienna ab initio simulation package (VASP) [28-30]. In the calculation of the plane waves, we used a cut-off energy of 350 eV, which was chosen by total energy convergence calculations for CeO_2 (111) and $Ce_{0.9}Gd_{0.1}O_2$ (111) slab systems. The CeO_2 (111) and $Ce_{0.9}Gd_{0.1}O_2$ (111) slab systems were initially constructed on a lattice with bulk CeO_2 bond lengths and then allowed to reach their lowest energy configurations by a relaxation procedure. Using this optimization procedure, the CeO_2 (111) slab system doped with gadolinium was investigated, and the charge transfer in CeO_2 (111) and $Ce_{0.9}Gd_{0.1}O_2$ (111) slab system was estimated. The surface was constructed as a slab within the three dimensional periodic boundary conditions: models are separated from their images in the direction perpendicular to the surface by a 14 Å vacuum layer. The simulated slab dimensions of CeO_2 (111) and $Ce_{0.9}Gd_{0.1}O_2$ (111) are 11.478 × 11.478 × 21.029 $Å^3$, and the simulated slab dimension of Gd (001) is 10.894 × 10.894 × 19.777 $Å^3$. For visualization and presentation purposes, Gaussian software was used. Bader charge analyses, were performed using the software provided at http://theory.cm.utexas.edu/vtsttools/bader/. The simulation graphics in this work were generated using XCrySDen [31, 32].The

bottom three layers were kept fixed to the bulk coordinates; full atomic relaxations were allowed for the top six layers. For these calculations, a 4 × 4 × 1 *k*-Point mesh was used in the 3 × 3 super cell. The atoms in the cell were allowed to relax until the forces on the unconstrained atoms were less than 0.01eV/Å.

3. RESULTS AND DISCUSSION

3.1 X-ray Diffraction and Rietveld Refinement Analyses

The crystallite structures of the prepared CeO_2 and 10GDC samples, analyzed by XRD, are shown in Fig. 1. The results reveal that the prepared samples had the cubic fluorite structures of CeO_2 and $Ce_{0.9}Gd_{0.1}O_{1.95}$, which are close to the standard JCPDS cards, respectively (CeO_2: #34-0394; $Ce_{0.9}Gd_{0.1}O_{1.95}$: #75-0161). In order to get precise structural insights into the synthesis materials during the APPJ process, all samples were verified by Rietveld refinement [33]. The points are the observed intensities and the line is the Rietveld fit. The background was corrected using a Chebyschev polynomial of the first kind and the diffraction peak profiles were fitted by Pseudo-Voigt function. Refined structural parameters along with the R-factors are listed in Table 1. The Rietveld parameters of R_{wp}, R_{exp}, and GOF for CeO_2 and 10GDC, are 4.82 and 3.15, 1.20 and 0.80, and 1.53 and 1.50, respectively. The Rietveld results indicated that a good agreement was obtained between the experimental relative intensities and the simulated intensities from the model. The calculated lattice constants of prepared CeO_2 and 10GDC are 5.411 and 5.417 Å, which are similar with the theoretical values of 5.416 and 5.418 Å, implying that Gd^{3+} ion evidently substituted into ceria lattice for the increase of lattice constant [34] by

APPJ process. The average crystallite sizes of prepared CeO_2 and 10GDC were found to be around 10.3 nm and 6.4 nm, respectively

3.2 Microstructure Analyses of CeO_2 and 10GDC

To learn the microscopic structure and morphology, we have performed the HR-TEM analysis and FFT images on the CeO_2 and 10GDC samples, the results are displayed in Fig. 2. The agglomeration of prepared CeO_2 and 10GDC is depicted in Figs. 2a-b, which indicates that the high surface energy among the NPs provided strong interactions (such as van der Waals forces) [35]. The lattice configuration of the sample is clearly shown in the HR-TEM image, which serves as the evidence that the prepared CeO_2 and 10GDC are quite crystalline. The d-spacing of 3.11 Å and 3.12 Å can be ascribed to the (111) crystal face of cubic phase CeO_2 and 10GDC. CeO_2 and 10GDC show nanostructural cubical and spherical shapes with the average particle sizes being approximately 10.5 nm and 6.7 nm by DLS analysis (see top right inset in Figs. 2a-b), which in a good agreement with the calculated crystalline size of XRD. As shown in the FFT images (Figs. 2c-d), all the diffraction spots are well indexed to cubic phases (111) and (200) planes. According to a molecular dynamics simulation by Sayle and co-workers, the favoured shape of a CeO_2 NP is a truncated octahedron, with exposed {110} and {111} faces [36]: the theoretical models studies provide compelling validation for our experimental studies.

The TEM-EDS spectrum (Fig. S1) taken from the same region reveals the characteristic peaks of O, Ce and Gd elements (the Cu signals are ascribed to the copper grid), suggesting the successful preparation of Gd-doped CeO_2 NPs by APPJ. In addition, the characteristic peak of nitrogen was not detected, indicating NO_3^- species from the initial precursor solution were not involved in the reaction with the metal ions to form nitrides or oxynitrides.

3.3 Electrochemical Impedance Analysis

Figure 3 shows the impedance spectra of the CeO_2 and 10GDC samples measured at 700 °C. Table 2 summarizes the grain conductivity, grain boundary conductivity, and total conductivity of these samples, which were obtained by fitting the measured impedance plots using the equivalent circuit shown in the inset of Fig. 3. In the equivalent circuit, R_g and R_{gb} represent the resistance corresponding to the ion conduction inside the grains and the resistance arising from the ion conduction at grain boundaries, respectively. The total ionic conductivity is calculated using following equations:

$$\sigma = \frac{l}{RA} \quad (1)$$

$$R_t = R_g + R_{gb} \quad (2)$$

where l is the pellet thickness, A is the area of electrodes, and R is the value of resistance obtained from fitting the impedance spectrum. The grain conductivity and

total conductivity were calculated using the grain resistance, R_g, and the total resistance, $R_g + R_{gb}$, respectively. From the results listed in Table 2, it can be seen that the grain conductivity is on the order of 10^{-6} and 10^{-4} S/cm for CeO_2 and 10GDC samples measured at 700 °C, respectively. As for the overall conductivity, a considerable increase in the overall conductivity from 2.3×10^{-4} S/cm to 4.2×10^{-2} S/cm is observed as Gd doped into CeO_2 lattice, implying that the improved ionic conductivity was attributed to the CeO_2 with Gd dopant.

3.4 Proposed Formation Mechanism of Nanoparticles by APPJ

To elucidate the final decomposition temperature of the powder product, the TGA/DTG spectra were recorded from the cerium nitrate hexahydrate ($Ce(NO_3)_3 \cdot 6H_2O$, 99%) and gadolinium nitrate hexahydrate ($Gd(NO_3)_3 \cdot 6H_2O$, 99%), as shown in Figs. 4a-d, respectively**.** The TGA curve of cerium nitrate hexahydrate (Fig. 4a) shows three major weight loss regions, the first and second peaks at around 157 °C and 224 °C, as seen in the DTG plot (Fig. 4b), can be mainly assigned to the dissociation of three and six water molecules in the cerium nitrate hexahydrate, resulting in further 12% and 26% weight loss and two peaks at 150 °C and 221 °C. The third weight loss starting around 293 °C corresponds to the decomposition of the anhydrous salt, which gives rise to a strong peak at 289 °C and a 57% weight loss. At temperatures in excess of 293 °C, no obvious weight loss was found, indicating an appropriate

decomposition temperature for the preparation of the powder product is 300 °C.

Gadolinium nitrate hexahydrate (Figs. 4c-d) follows a different pattern when heated. The two inflection points in the weight loss curve at about 169 °C and 255 °C should correspond to the 11% and 21% weight loss of crystalline water, respectively. The 21% of total weight loss at 255 °C is very close again to the stoichiometric amount corresponding to subtraction of six water molecules (i.e., 24%). Decomposition of the anhydrous salt seems to occur in two stages starting at about 353 °C and reaching a plateau at 405 °C. This plateau corresponds to a total weight loss of about 49%. The second process starts at about 475 °C reaching a second plateau at about 521 °C at which a 57% total weight loss is recorded. From 521 to 672 °C, an additional gradual weight loss of 3% results in a total weight loss close to the stoichiometric conversion value to Gd_2O_3 (i.e., 60%).

Evaluation of plasma temperatures for generation of NPs is an important step in the APPJ process. Figure S2 shows the temperature evolutions for the APPJ process at various powers. The results indicated that the temperature increased rapidly from 0 to 15 s and then became steady, which were approximately 323, 425, and 674 °C at 300, 400, and 500 W, respectively. According to the above results, the final decomposition temperature of gadolinium nitrate hexahydrate (672 °C) was below the plasma temperature of 300 W (323 °C), implying that the decomposition temperature was not

sufficient to produce Gd_2O_3 at 300 W, and to further react with CeO_2 to form GDC NPs. For the traditional fabrication of a single 10GDC phase [37-39], the calcined temperatures of synthesis methods mainly rely on the decomposition temperatures of initial precursors and the reaction temperature between Gd_2O_3 and CeO_2. As a result, we predicted that the formation of oxidized products is related to the chemical reactions inside the plasma region in an APPJ system.

To gain further insight into the mechanism of particle synthesis and to identify the reactive plasma species involved in the plasma exposure, the plasma analysis was performed by optical emission spectroscopy. The spectral characteristics between 200-900 nm (dry air plasma) with the atomized precursors transferred by O_2 carrier gas were plotted - see Figure S3. The spectral lines were identified using NIST reference data [40]. Within the 200-450 nm range, the spectral features in dry air are referred to the main emitted peaks of N_2, N_2^+, and NO. Due to dry air being composed of 78.09% nitrogen gas, the spectrum showed a second positive system of the nitrogen molecule (N_2, $C^3\Pi_u$-$B^3\Pi_g$, 290-410 nm), the first negative system of the nitrogen molecular ion (N_2^+, $B^2\Sigma_u$-$X^2\Sigma_g$, 330-450 nm), and the nitric oxide γ-system (NO, $A^2\Sigma$-$X^2\Pi$, 220-290 nm) [41-45].

According to the results of TEM-EDS (Fig. S1), the characteristic peak of nitrogen was not detected, indicating excited nitrogen-related species were not

involved in the reaction with the metal ions to form nitrides or oxynitrides. However, the excited peaks of O_2^+ and O* located at a range between 450 and 900 nm play important active species in the reactions of air plasma. The first negative systems of O_2^+ (O_2^+, $b^4\Sigma_g$-$a^4\Pi_u$, 450-700 nm) and oxygen radicals (O*, $3p^5P$–$3s^5S^0$ and $3p^3P$–$3s^3S^0$, 777.34 and 845.46 nm) were also detected in the spectrum [46]. The production of oxygen radicals as a strong oxidative agent in the APPJ processes was considered to be the oxygen source reacting with metal ions inside the atomize droplets to form the oxidized product in this study. In addition, the presence of cerium and gadolinium species was not detected, which can be attributed to the lower concentration of the initial precursors.

By considering the above results, a schematic mechanism responsible for the formation from the precursor solution by the APPJ process has been proposed and is shown in Fig. 5. First, the mixture of gadolinium nitrate and cerium nitrate as precursor was dissolved in de-ionized water to form an ionized homogeneous solution, which was subsequently atomized to form the atomized droplets for the further transportation to the plasma jet by O_2 carrier gases. The average diameter of the atomized droplets can be determined using Lang's equation [47] on the assumptions that waves of spherical diameter are created and that the liquid velocity at the sides of the dish is equal to zero.

$$d_{droplet} = 0.34\left(\frac{8\pi r}{\rho f^2}\right)^{\frac{1}{3}} \quad (8)$$

where $d_{droplet}$ is the atomized droplet diameter (μm), r is the surface tension of pure water (72.9 mN $\cdot$ m^{-1}), ρ is the solution density (1030.3 kg $\cdot$ m^{-3}), and f is the ultrasonic frequency of the piezoelectric ceramic oscillator (2.45 MHz). The diameter of the atomized droplets calculated using the above parameters was found to be 2.27 μm. An atomized droplet can be viewed as numerous metal ions in each droplet being present by the weight percentage concentration of the initial precursors. The calculated number is 1.8×10^8 metal ions in each droplet. Based on above results, it is believed that predominantly nanosized CeO_2 and 10GDC particles were formed by the gas-to particle mechanism, due to the nucleation of particles from gas phase [48]. An obvious difference in diameter between the atomized droplet and prepared particles was confirmed as the atomized droplets decomposed into NPs and underwent a reduction of size due to the evaporation-decomposition of water and disolved nitrate ions ($NO_3^-{}_{(aq)} \rightarrow NO_{X(g)}$), in-flight reaction, melting and solidification. Furthermore, most metal elements are available as dissolved nitrate salts in aqueous solution. The atmospheric pressure plasma process generated oxygen-related as strong oxidative agents caused the metal ions to form the oxidized product. Based on our results and the proposed mechanism, APPJ process can be utilized as a fast oxidation process to achieve one-step fabrication of CeO_2 and 10GDC nanoparticles, as well as the

functional oxide materials for other applications.

3.5 DFT calculation and Bader charge analyses

In order to understand the sharp increase in the electrical performance of 10GDC, we have investigated their Bader charge variation. From experiment observation and density functional theory (DFT) study, the conductivity of 10GDC is higher than that of CeO_2 contributed to the improvement of the clear charge transfer by the electronic effect. The DFT computations were performed for the CeO_2 (111), Gd (001), and $Ce_{0.9}Gd_{0.1}O_2$ (111) systems in order to interpret the observed phenomena of variation in efficiency in the following section. For studying Gd-doping CeO_2 issues such as charge transfer, an appropriate surface model has been determined with much care. To discuss the electronic structure effects on the CeO_2 (111) and $Ce_{0.9}Gd_{0.1}O_2$ (111) systems, the slab model approaches have been respectively employed as the surface models. For modeling the CeO_2 (111) molecules, and $Ce_{0.9}Gd_{0.1}O_2$ (111) and Gd (001) slab surfaces, we have adopted slabs as shown in Figs. 6a-c.

The Bader charge analyses were carried out for CeO_2 (111), $Ce_{0.9}Gd_{0.1}O_2$ (111), Gd (001) to examine the charge transfer between Ce-O and Gd atoms, and the charge results are listed in Table 3. In the $Ce_{0.9}Gd_{0.1}O_2$ (111) system, the charge of oxygen was increased from 7.3016 e (for the bare CeO_2 (111)) to 7.3534 e. This is

quite reasonable that the donation of charge of Gd atom as doped metal to oxygen would easily occur. Since Ce has a less electronagativity (1.1) than that for oxygen (3.5), greater electron donation to O from Gd atom of the doping metal than that from Ce can be inferred. All these factors severely reduce effective bonding between the Gd and Ce-O. Thus, the present study clearly demonstrates that the improved charge transfer of Gd-doped CeO_2 mainly arises due to the higher value of Bader charge, implying that an electronic effect plays an important role for improving ionic conductivity of $Ce_{0.9}Gd_{0.1}O_2$ system. Figure 6 illustrates the activity dependence on charge donation in $Ce_{0.9}Gd_{0.1}O_2$. At present, we are interested in a preliminary estimation of how atomic charges may change with the Gd dopant. Therefore, we believe that the CeO_2 (111) surface doped with Gd metal could play an important role in the electrochemical reaction of SOFCs.

4. CONCLUSIONS

We report a novel technology using an atmospheric pressure plasma jet (APPJ) for the preparation of CeO_2 and 10GDC NPs. Several advantages in this fabrication, such as one-step fabrication without by-products, fast oxidation process of the obtained product and achieving the high temperature phase through plasma chemical reactions allowed us to synthesize pure and multicomponent nano-sized particles. Therefore, the preparation of various NPs using the APPJ system could be used as a new alternative of a low cost fabrication.

The most important discovery is that controlling the alloying extent of Gd represents a promising approach to improve the ionic conductivity by Bader charge analyses for SOFCs applications. A better understanding of this interaction will facilitate the design of better conjugates for $Ce_{0.9}Gd_{0.1}O_2$ nanocrystals for various applications.

ACKNOWLEDGMENT

The authors would like to thank Mr. Sheng-Chung Liao of the Instrument Center for the kind assistance in FE-SEM, and Mr. Jian-Ming Chiu of Chemical Engineering department for the technical assistance in HR-TEM at the National Taiwan University of Science and Technology.

REFERENCE

[1] J. A. Kilner and R. J. Brook, *Solid State Ionics* 1982, **6**, 237-252.

[2] D. J. Kim, *J. Am. Ceram. Soc.*1989, **72**, 1415-1421.

[3] S. Omar, E. D. Wachsman, J. L. Jones and J. C. Nino, *J. Am. Ceram. Soc.* 2009, **92**, 2674-2681.

[4] B. C. H. Steele and A. Heinzel, *Nature*, 2001, **414**, 345-352.

[5] B. C. H. Steele, *Solid State Ionics*, 2000, **129**, 95-110.

[6] T. Kudo and H. Obayashi, *J. Electrochem. Soc*., 1975, **122**, 142-147.

[7] R. Gerhardt-Anderson and A. S. Nowick, *Solid State Ionics*, 1981, **5**, 547-550.

[8] H. Yahiro, Y. Baba, K. Eguchi and H. Arai, *J. Electrochem. Soc*., 1988, **135**, 2077-2080.

[9] J. A. Rodriquez and D. W. Goodman, *Science*, 1993, **260**, 1527-1528.

[10] C. Y. Tai, J. L. Chang, J. F. Lee, T. S .Chan and J. M. Zen, *Electrochim. Acta*, 2011, **56**, 3115-3121.

[11] R. Sardar, A. M. Funston, P. Mulvaney and R. W. Murray, *Langmuir*, 2009, **25 (24)**, 13840-13851.

[12] J.-Y. Park, Y.-J. Lee, P. R. Karandikar, K.-W. Jun, K.-S. Ha and H.-G. Park, *Appl. Catal. A: Gen.*, 2012, **411-412**, 15-23.

[13] Z. Liu, M. Shamsuzzoha, E. T. Ada, W. M. Reichert and D. E. Nikles, *J. Power*

Sources, 2007, **164**, 472-480.

[14] K. Higashi, K. Sonoda, H. Ono, S. Sameshima and Y. Hirata, *J. Mater. Res.*, 1999, **14**, 957-967.

[15] K. Huang, M. Feng, J. B. Goodenough, *J. Am. Ceram. Soc*., 1998, **81**, 357-362.

[16] K. Yamashita, K. V. Ramanujachary and M. Greenblatt, *Solid State Ionics*, 1995, **81**, 53-60.

[17] R. O. Fuentes and R. T. Baker, *Journal of Power Sources*, 2009, **186**, 268-277.

[18] Y. W. Hsu, H. C. Li, Y. J. Yang and C. C. Hsu, *Thin Solid Films*, 2011, **519**, 3095-3099.

[19] M. C. Kim, S. H. Yang, J.-H. Boo and J. G. Han, *Surf. Coat. Tech.*, 2003, **174-175**, 839-844.

[20] P. A. Lin and R. M. Sankaran, *Angew. Chem. Int. Ed.*, 2011, **123**, 11145-11148.

[21] D. Vanderbilt, *Phys. Rev. B: Condens. Matter*, 1990, **41**, 7892-7895.

[22] P. E. Blochl, *Phys. Rev. B: Condens. Matter*, **1994**, *50*, 17953-17979.

[23] M. C. Payne, M. P. Teter, D. C. Allan, T. A. Arias and J. D. Joannopoulos, *Rev. Mod. Phys.***1992**, *64*, 1045-1097.

[24] G. Kresse and D. Joubert, *Phys. Rev. B: Condens. Matter*, 1999, **59**, 1758-1775.

[25] P. Hu, D. A. King, S. Crampin, M. H. Lee and M. C. Payne, *Chem. Phys. Lett*., 1994, **230**, 501-506.

[26] J. P. Perdew, J. A. Chevary, S. H. Vosko, K. A. Jackson, M. R. Pederson, D. J. Singh and C. Fiolhais, *Phys. Rev. B: Condens. Matter* 1992, **46**, 6671-6687.

[27] J. P. Perdew, in *Electronic Structure of Solids '91*, ed. P. Ziesche and H. Eschrig, Akademie Verlag, Berlin, 1991.

[28] G. Kresse and J. Hafner, *J. Phys. Rev. B: Condens. Matter*, 1993, **47**, 558-561.

[29] G. Kresse and J. Furthmüller, *J. Phys. Rev. B: Condens. Matter*, 1996, **54**, 11169-11186.

[30] G. Kresse and J. Furthmüller, *Comput. Mat. Sci*., 1996, **6**, 15-50.

[31] A. Kokalj, *Comput. Mat. Sci*., 2003, **28**, 155-168.

[32] A. Kokalj, *J. Mol. Graphics Modelling*, 1999, **17**, 176-179.

[33] R. A. Young, in *The Rietveld Method (International Union of Crystallography)*, ed. R. A. Young, Oxford University Press, New York, 1996.

[34] T. S. Zhang, J. Ma, S. H. Chan, P. Hing and J. A. Kilner, *Solid State Sciences*, 2004, **6**, 565-572.

[35] G. A. Rance, D. H. Marsh, S. J. Bourne, T. J. Reade and A. N. Khlobystov, *ACS Nano*, 2010, **4 (8)**, 4920-4928.

[36] D. C. Sayle, S. A. Maicaneanu and G. W. Watson, *J. Am. Chem. Soc*., 2002, **124 (38)**, 11429-11439.

[37] A. Sin, Y. Dubitsky, A. Zaopo, A. S. Arico, L. Gullo, D. L. Rosa, S. Siracusano,

V. Antonucci, C. Oliva and O. Ballabio, *Solid State Ionics*, 2004, **175**, 361-366.

[38] T. S. Zhang, J. Ma, S. H. Chan and J. A. Kilner, *Solid State Ionics*, 2005, **176**, 377-384.

[39] J. G. Cheng, S. W. Zha, J. Huang, X. Q. Liu and G. Y. Meng, *Mater. Chem. Phys.*, 2003, **78**, 791-795.

[40] National Institute of Standards and Technology, http://www.nist.gov/pml/data/asd.cfm, (accessed September 2014)

[41] F. U. Khan, N. U. Rehman, S. Naseer, M. A. Naveed, A. Qayyum, N. A. D. Khattak and M. Zakaullah, *Eur. Phys. J. Appl. Phys*., 2009, **45**, 11002-11009.

[42] T. Sakamoto, H. Matsuura and H. Akatsuka, *J. Appl. Phys.*, 2007, **101**, 23307-23317.

[43] V. Linss, H. Kupfer, S. Peter, F. Richter, *J. Phys. D: Appl. Phys.* 2004, **37**, 1935-1944.

[44] A. Fridman, in *Plasma Chemistry*, Cambridge University Press, Cambridge, 2008.

[45] S. C. Hill and L. D. Smoot, *Prog. Energy Combust. Sci.* 2000, **26 (4-6)**, 417-458.

[46] D. R. Bates and A. Dalgarno, in *Atomic and Molecular Processes*, ed. D. R. Bates, Academic Press, New York, 1962.

[47] R. J. Lang, *J. Acoust. Soc. Am.* **1962**, *34 (1)* 6-8.

[48] T.T. Kodas and M.J. Hampden-Smith, in *Aerosol processing of materials*, Wiley-Vch, New York, 1999.

FIGURE CAPATIONS

Figure 1 Rietveld refinement analyses for XRD spectra of prepared (a) CeO_2 and (b) 10GDC by APPJ.

Figure 2 HR-TEM images, FFT pattern and particle size distribution of prepared (a, c) CeO_2 and (b, d) 10GDC nanoparticles by APPJ.

Figure 3 Impedance spectra of CeO_2 and 10GDC pellets were measured at 700 °C.

Figure 4 The TGA/DTG analysis results of (a) weight loss and (b) differential versus temperature for $Ce(NO_3)_3 \cdot 6H_2O$ precursor; (c) weight loss and (d) differential versus temperature for $Gd(NO_3)_3 \cdot 6H_2O$ precursor.

Figure 5 Proposed formation mechanism of nanoparticles from atomized solution droplets into an APPJ process.

Figure 6 Bader charge analyses of CeO_2 (111) and $Ce_{0.9}Gd_{0.1}O_2$ (111) and Gd (001) systems.

SUPPLEMENTARY FIGURES CAPATIONS

Figure S1 TEM-EDS pattern of prepared (a) CeO_2 and (b) 10GDC particles.

Figure S2 Plasma temperatures at 300, 400, and 500 W.

Figure S3 Optical emission spectra of the CDA plasma with atomized precursors and O_2 carrier gas.

TABLE CAPATIONS

Table 1 Crystallographic data and structural refinements of CeO_2 and 10GDC prepared by APPJ.

Table 2 The grain conductivity, grain boundary conductivity and total conductivity of CeO_2 and 10GDC measured at 700 ℃.

Table 3 Bader charge analyses of CeO_2 (111) and $Ce_{0.9}Gd_{0.1}O_2$ (111) and Gd (001) systems.

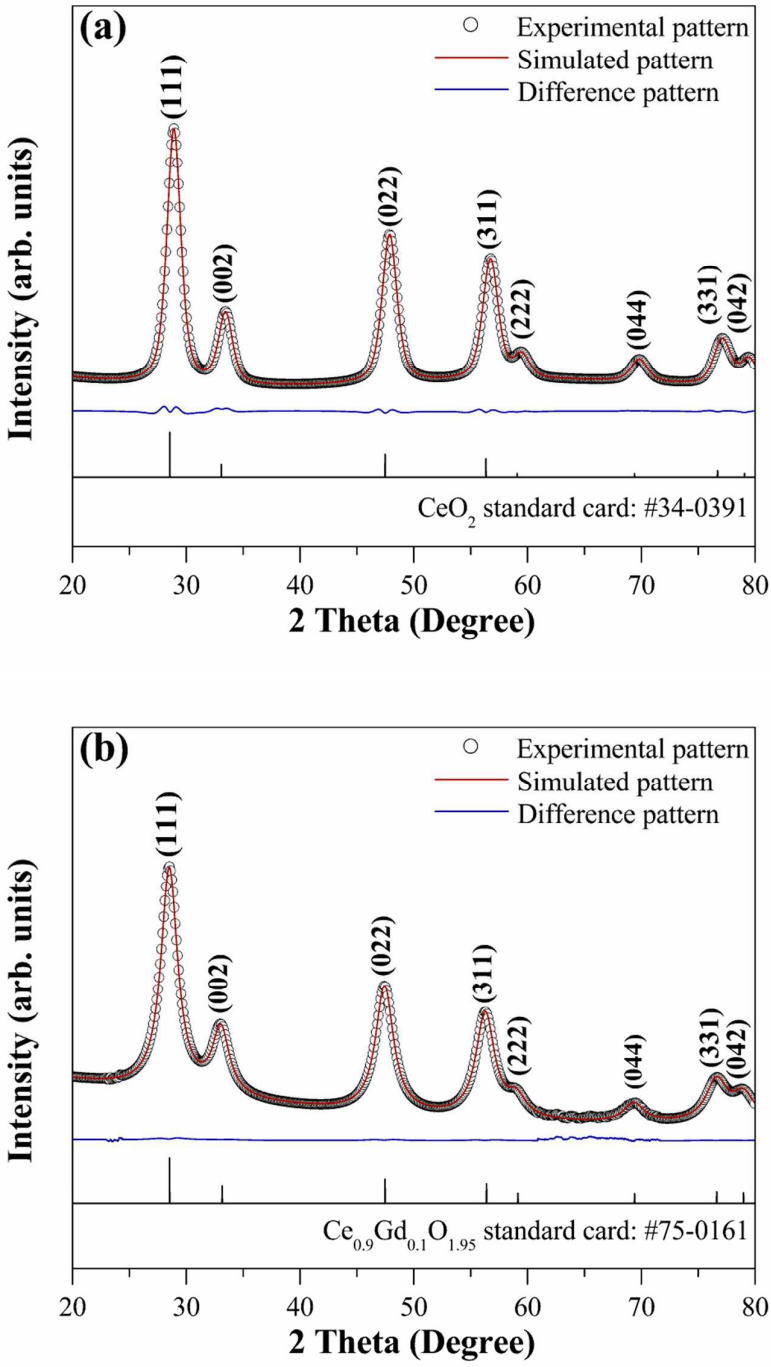

Figure 1

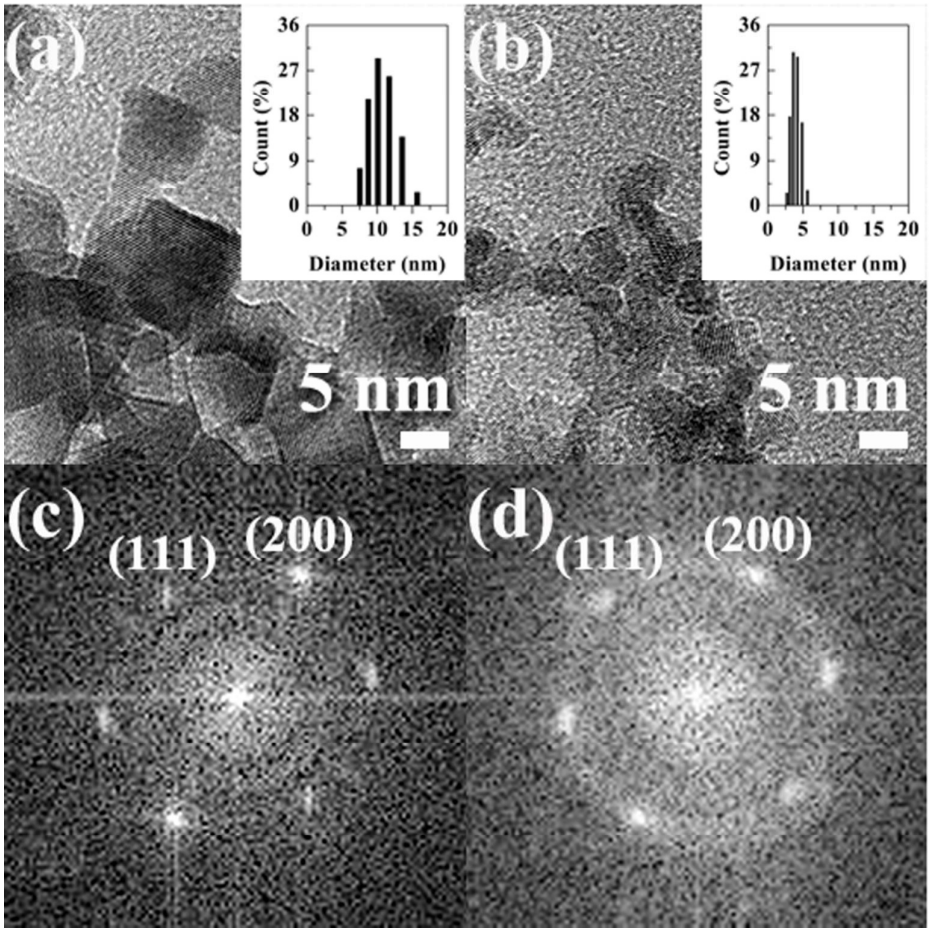

Figure 2

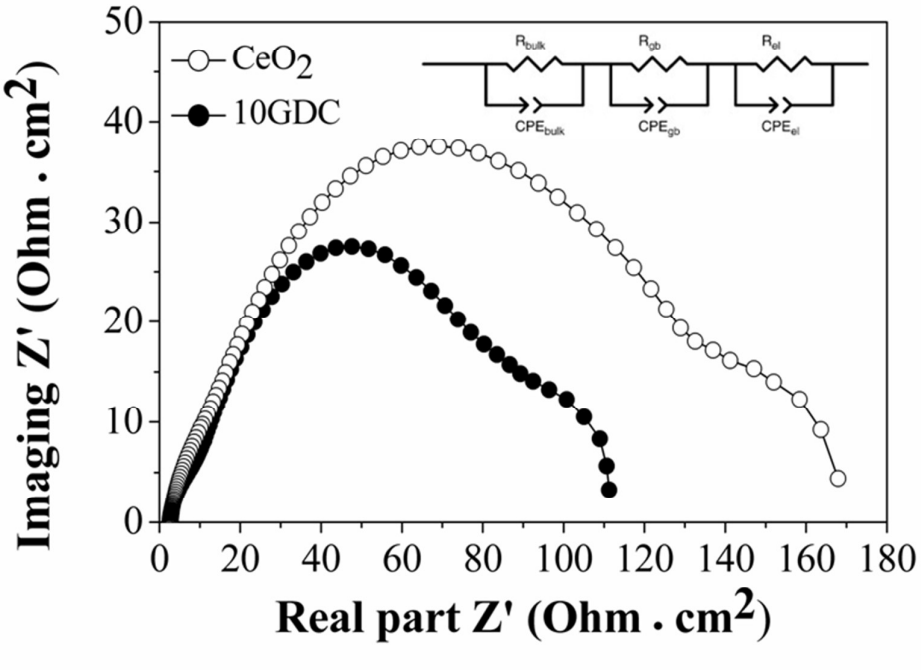

Figure 3

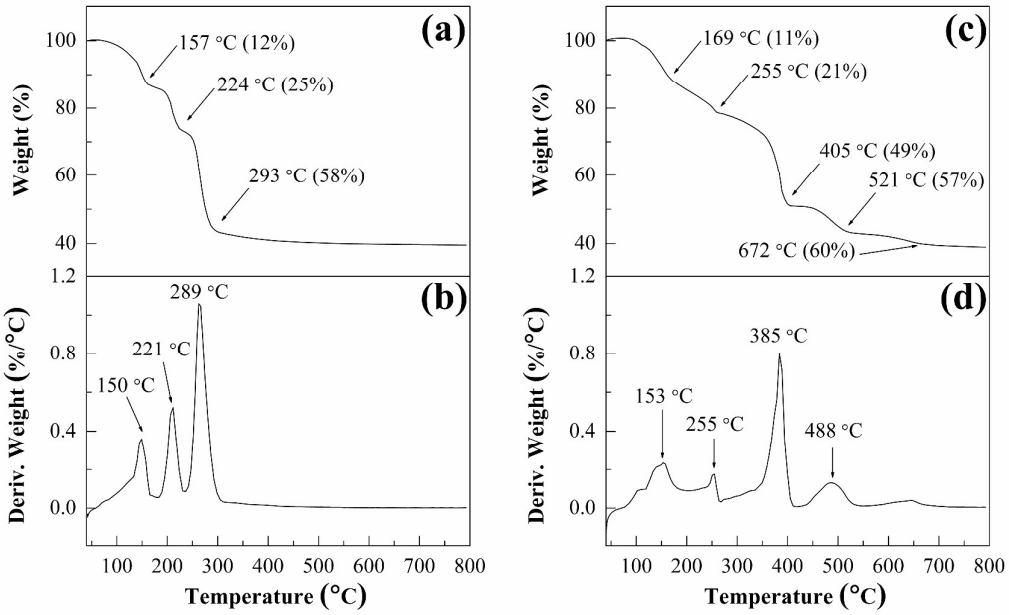

Figure 4

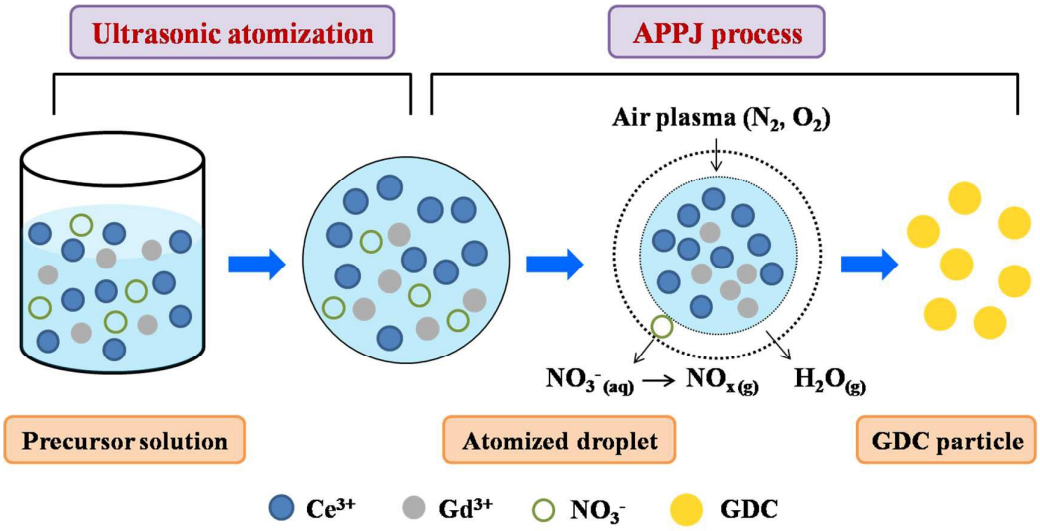

Figure 5

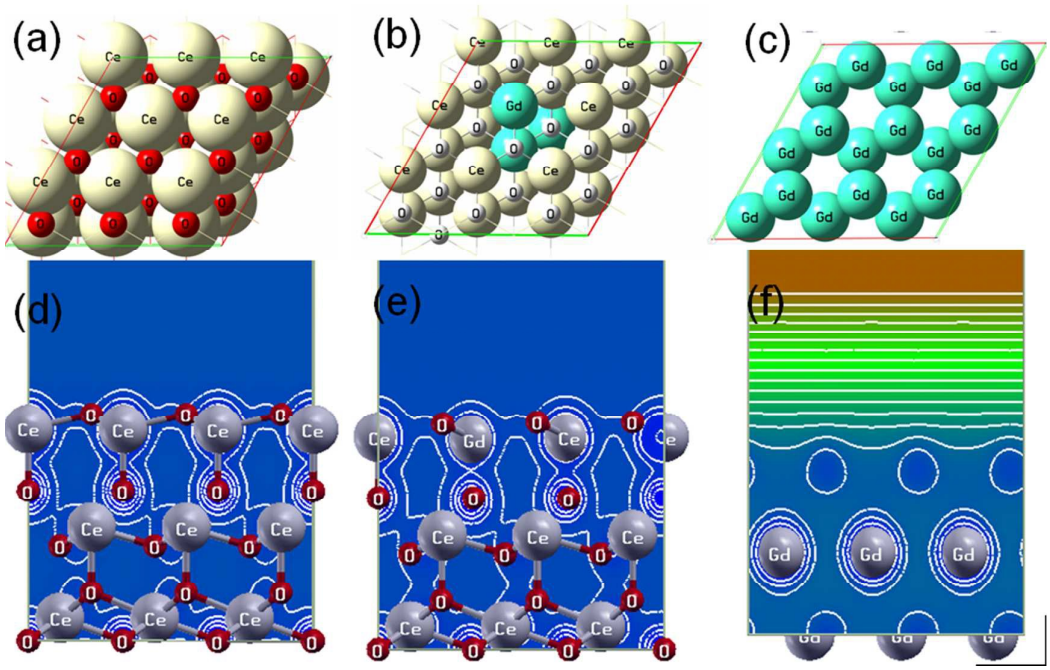

Figure 6

Table 1

Composition	**CeO_2**	**$Ce_{0.9}Gd_{0.1}O_{1.95}$**
Space Group	Fm3m	Fm3m
R_{wp} (%)	4.82	1.20
R_{exp} (%)	3.15	0.80
GOF	1.53	1.50
a (Å)	5.411	5.417
Cell volume ($Å^3$)	158.45	159.26
Unit cell density (g/cm^3)	7.215	7.216
Crystallite Size (nm)	10.3	5.3

Table 2

Sample	Grain Conductivity (S/cm)	Grain Boundary Conductivity (S/cm)	Total Conductivity (S/cm)
CeO_2	4.7×10^{-6}	6.1×10^{-5}	2.3×10^{-4}
10GDC	2.6×10^{-4}	7.3×10^{-3}	4.2×10^{-2}

All samples were sintered at 1500°C

Table 3

Species	Charge (e)	Charge difference (e)
CeO_2 (111)	Ce: 9.8486	-
	O: 7.3016	
Gd(001)	Gd: 8.993	
$Ce_{0.9}Gd_{0.1}O_2$(111)	Ce: 9.8461	Ce: 9.8486−9.8461 = +0.0005
	O: 7.3534	O: 7.3016−7.3534 = -0.0518
	Gd: 6.800	Gd: 8.993-6.800 = + 2.193